

Measurement and prediction of the relationship between capillary pressure, saturation, and interfacial area in a NAPL-water-glass bead system

Mark L. Porter,¹ Dorthe Wildenschild,¹ Gavin Grant,² and Jason I. Gerhard³

Received 28 January 2009; revised 3 March 2010; accepted 10 March 2010; published 6 August 2010.

[1] In this work, the constitutive relationship between capillary pressure (P_c), saturation (S_w), and fluid-fluid interfacial area per volume (IFA) is characterized using computed microtomography for drainage and imbibition experiments consisting of a nonaqueous phase liquid and water. The experimentally measured relationship was compared to a thermodynamic model that relates the area under the $P_c - S_w$ curve to the total IFA, a_n , and the capillary-associated IFA, a_{nw} . Surfaces were fit to the experimental and modeled $P_c - S_w - a_n$ and $P_c - S_w - a_{nw}$ data in order to characterize the relationship in three dimensions (3D). For the experimental system, it was shown that the $P_c - S_w - a_n$ relationship does not exhibit hysteresis. The model is found to provide a reasonable approximation of the magnitude of the 3D surfaces for a_n and a_{nw} , with a mean absolute percent error of 26% and 15%, respectively. The relatively high mean absolute percent errors are primarily the result of discrepancies observed at the wetting- and nonwetting-phase residual saturation values. Differences in the shapes of the surfaces are noted, particularly in the curvature (arising from the addition of scanning curves and presence of $a_n - S_w$ hysteresis in the predicted results) and endpoints (particularly the inherent nature of thermodynamic models to predict significant a_{nw} associated with residual nonwetting-phase saturation). Overall, the thermodynamic model is shown to be a practical, inexpensive tool for predicting the $P_c - S_w - a_n$ and $P_c - S_w - a_{nw}$ surfaces from $P_c - S_w$ data.

Citation: Porter, M. L., D. Wildenschild, G. Grant, and J. I. Gerhard (2010), Measurement and prediction of the relationship between capillary pressure, saturation, and interfacial area in a NAPL-water-glass bead system, *Water Resour. Res.*, 46, W08512, doi:10.1029/2009WR007786.

1. Introduction

[2] Fluid-fluid interfacial area (IFA) plays a critical role in many subsurface multiphase flow and transport processes. Two distinct contributions to the total fluid-fluid IFA, a_n , have been identified in the literature. These include capillary-associated IFA, a_{nw} , and film-associated IFA. Capillary-associated IFA includes all nonwetting interfaces in contact with the bulk, mobile wetting-phase and wetting-phase pendular rings, whereas film-associated IFA consists of the nonwetting-phase in contact with the wetting-phase films that exist on solids of pores occupied by the nonwetting-phase [Gladkikh and Bryant, 2003]. Figure 1 illustrates the fluid-fluid interfacial area distinguished in the two-fluid porous media system addressed in this work. The distinction between a_n and a_{nw} relies on the ability of a particular measurement technique to resolve the different components of the

wetting-phase [Bryant and Johnson, 2004], which will be discussed further in the following paragraphs.

[3] In the past decade, a number of investigations have focused on the characterization and validation of the constitutive relationship between capillary pressure, P_c , wetting-phase saturation, S_w , and a_{nw} proposed by Hassanizadeh and Gray [1993]. This relationship is an extension of the traditional $P_c - S_w$ constitutive relationship, in which it is assumed that the macroscale variables P_c and S_w uniquely describe the microscale physics of the system. Although the traditional approach is useful for modeling purposes, concerns have been raised regarding its shortcomings [e.g., Hassanizadeh and Gray, 1993; Miller et al., 1998; Muccino et al., 1998; Gray, 2000]. Furthermore, modeling complexities arise since hysteresis exists between drainage and imbibition events. In an effort to better represent the microscale physics, Hassanizadeh and Gray [1993] expanded the functional dependence of the $P_c - S_w$ relationship to include a_{nw} , which explicitly accounts for the numerous fluid-fluid interfacial configurations that may exist for any given S_w value. In addition, Hassanizadeh and Gray [1993] hypothesized that the inclusion of a_{nw} in the macro-scale formulation of P_c would account for hysteresis observed in the traditional $P_c - S_w$ relationship (i.e., a single 3D surface exists in $P_c - S_w - a_{nw}$ space).

¹School of Chemical, Biological, and Environmental Engineering, Oregon State University, Corvallis, Oregon, USA.

²Geosyntec Consultants, Guelph, Ontario, Canada.

³Department of Civil and Environmental Engineering, University of Western Ontario, London, Ontario, Canada.

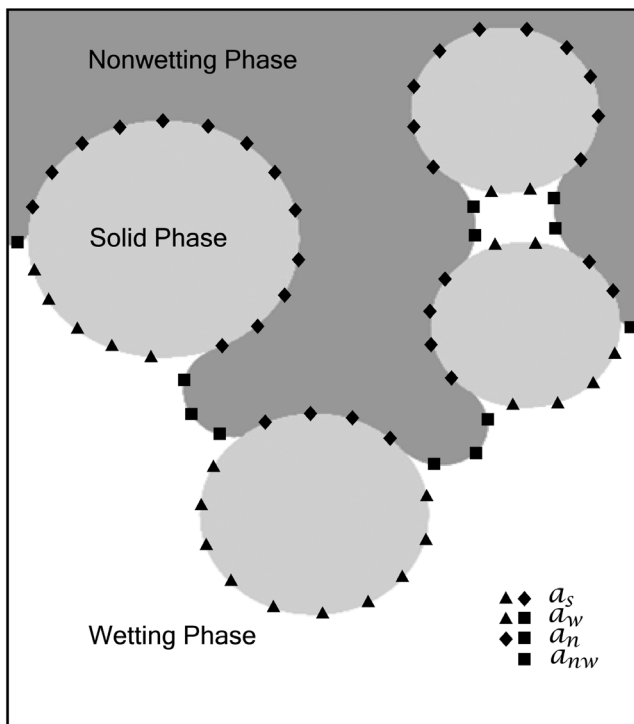


Figure 1. Illustration of the interfacial areas defined for the two-fluid porous system addressed in this work.

[4] Experimental investigations focused on simultaneously measuring P_c , S_w , and fluid-fluid IFA in porous media are often difficult, expensive, and subject to limitations, thus only a few have been reported in the literature [e.g., Cheng *et al.*, 2004; Culligan *et al.*, 2004, 2006; Brusseau *et al.*, 2006; Chen and Kibbey, 2006; Chen *et al.*, 2007]. Cheng *et al.* [2004] and Chen *et al.* [2007] conducted drainage and imbibition experiments (S_w values ranging from 0.4 to 1.0) in a thin porous micromodel and analyzed two-dimensional (2D) images of the fluid configurations within the pores to obtain a_{nw} estimates. In both cases the maximum magnitude of the surfaces ranged from approximately $2.0\text{--}4.5\text{ mm}^{-1}$, while exhibiting convex curvature along the S_w -axis and relatively little curvature along the P_c -axis (except at high S_w values where a slight convex curvature exists). Culligan *et al.* [2004, 2006] used computed microtomography (CMT) to quantify a_{nw} for air-water and NAPL-water drainage and imbibition column experiments; however, these studies focused on characterizing $a_{nw} - S_w$ curves and did not directly address the $P_c - S_w - a_{nw}$ relationship. Brusseau *et al.* [2006] related independent measurements of $P_c - S_w$ and interfacial tracer technique (IFTT) measurements of a_n for statistically similar porous media, but did not investigate $P_c - S_w - a_n$ in 3D. Chen and Kibbey [2006] used IFTT to investigate the $P_c - S_w - a_n$ relationship in 3D; however, they only measured a_n during drainage. The above literature review clearly indicates that there is a need for further experimental studies focused on characterizing the relationship between $P_c - S_w - a_n$ and $P_c - S_w - a_{nw}$, particularly for NAPL-water systems.

[5] In lieu of experimental data, pore scale numerical modeling techniques have proven to be a useful tool for investigating the $P_c - S_w - a_{nw}$ relationship. A number of works have focused on pore network modeling, which have

resulted in a variety of characteristics for the $P_c - S_w - a_{nw}$ relationship [Reeves and Celia, 1996; Held and Celia, 2001; Joekar-Niasar *et al.*, 2007; Helland and Skjæveland, 2007; Joekar-Niasar *et al.*, 2009]. Reeves and Celia [1996] presented a surface that exhibited notable convex curvature along both the S_w - and P_c -axis, whereas the surfaces presented by Held and Celia [2001] and Joekar-Niasar *et al.* [2007] exhibited a slight concave curvature along the P_c -axis at higher S_w values. Helland and Skjæveland [2007] investigated the effect of mixed wet media on the $P_c - S_w - a_{nw}$ relationship and showed that the shape of the surface was sensitive to contact angle hysteresis. Recently, Joekar-Niasar *et al.* [2009] successfully simulated the non-hysteretic $P_c - S_w - a_{nw}$ experiments reported by Chen *et al.* [2007], which exhibited negligible curvature along the P_c -axis. Lattice-Boltzmann simulations of the $P_c - S_w - a_{nw}$ relationship were also recently reported [Porter *et al.*, 2009], and the results showed that the modeled surface exhibited convex curvature along the S_w -axis, while there was negligible curvature along the P_c -axis.

[6] Thermodynamic considerations suggest that a_n is proportional to the work of fluid displacement as estimated by the area under the $P_c - S_w$ curve [Leverett, 1941; Morrow, 1970]. Although originally employed for predicting $a_n - S_w$ during nonwetting-phase displacing wetting-phase (i.e., drainage), this approach has been further developed for estimating (1) $a_n - S_w$ during imbibition [Bradford and Leij, 1997], (2) a_n at residual NAPL saturation [Dobson *et al.*, 2006], and (3) a_n for any S_w value when the saturation history is known [Grant and Gerhard, 2007a; Schroth *et al.*, 2008]. While the thermodynamic method estimates a_n , heuristic conversion to a_{nw} can be achieved by employing, for example, a_{nw}/a_n functions from the literature and accounting for the energy dissipation associated with non-reversible capillary instabilities [Grant and Gerhard, 2007a]. The Grant and Gerhard [2007a] model (hereafter, Explicit IFA model) for predicting $a_{nw} - S_w$ was demonstrated to provide reasonable approximations of measured data sets [Culligan *et al.*, 2004, 2006] without any calibration to the data [Grant and Gerhard, 2007a]. Such models, once validated, provide a relatively simple method to estimate a_n and a_{nw} , and thereby avoid the expense of direct measurement. Furthermore, the dependence of a_n and a_{nw} on $P_c - S_w$ functions, which are already embedded in multiphase flow simulators, can provide a straightforward and reliable means to simulate processes that depend on IFA (e.g., nonwetting-phase dissolution) without resorting to lumped mass transfer coefficients [Grant and Gerhard, 2007b]. However, rigorous validation for these models has been limited by lack of appropriate data [Schroth *et al.*, 2008]. To the authors' knowledge, thermodynamic models have not been evaluated for their ability to predict $P_c - S_w - a_n$ or $P_c - S_w - a_{nw}$ surfaces.

[7] The objective of this study is to directly measure P_c , S_w , a_n , and a_{nw} during drainage and imbibition and compare observations with those predicted from a thermodynamic model. These direct measurements are used to establish $P_c - S_w - a_n$ and $P_c - S_w - a_{nw}$ relationships. The comparison between observations and predictions provides insight into the value of thermodynamic models to provide reasonable approximations of $P_c - S_w - a_n$ and $P_c - S_w - a_{nw}$. We also highlight aspects of CMT image analysis that distinguish bulk wetting-phase funicular patterns from pendular rings.

Table 1. Size Distribution of Soda Lime Beads

Percent Weight	Diameter (mm)
0.35	0.6
0.35	0.8
0.30	1.0–1.4

The differentiation of these separate wetting-phase morphologies allows for more detailed characterization of the experimental data and quantification of the amount of wetting-phase associated with each morphology.

2. Methods

2.1. NAPL-Water Experiments

[8] The drainage and imbibition experiments presented here were carried out at the GeoSoilEnviro Consortium for Advanced Radiation Sources (GSECARS) bending magnetic beamline, Sector 13, Advanced Photon Source (APS), Argonne National Laboratory. A detailed description of synchrotron CMT is beyond the scope of this work; details regarding CMT applied to similar multiphase systems can be found in the works of *Wildenschild et al.* [2002, 2005], *Culligan et al.* [2004, 2006], and *Porter and Wildenschild* [2010, and references therein].

[9] The experiments were conducted in a glass column (inside diameter = 7.0 mm; length = 25.0 mm) packed with soda-lime glass beads ($\rho = 2.5 \text{ g/cm}^3$). The size distribution of the bead diameters are provided in Table 1. A semi-permeable, hydrophilic membrane (Nylaflo Nylon Membrane, $0.2 \text{ }\mu\text{m}$) was placed at the bottom of the column to prevent NAPL from entering the water line. The water line was connected to a syringe pump (Gilson 402, Gilson Inc.), which precisely controlled ($\pm 1.0 \text{ }\mu\text{l}$) the amount of water pumped into and out of the porous medium. A small rubber stopper containing a NAPL outlet tube connected to a reservoir was placed inside the column in contact with the top of the porous medium. The NAPL used in this study was Soltrol 220 (Chevron Philips, $\rho = 0.79 \text{ g/cm}^3$) dyed red with Oil Red O (Sigma Aldrich) and the interfacial tension was 0.0378 N/m [*Schaap et al.*, 2007]. The water was doped

with KI at a 1:6 mass ratio of KI:H₂O, which increased the contrast between the water and NAPL phases in the CMT images. The pressure of each phase was measured (Validyne P55 Differential Pressure Transducer) in the fluid lines above and below the porous medium throughout the entire experiment. A quasi-static point on the $P_c - S_w$ curve was obtained by pumping a precise amount of water into (imbibition) or out of (drainage) the column at a flow rate of 0.6 ml/hr , shutting off the pump and then waiting for 15 minutes to allow for the system to equilibrate. It is expected that this equilibration time is appropriate for $S_w > 0.5$, although it is known that pressure equilibrium after a saturation change tends to increase with decreasing S_w [*Gerhard and Kueper*, 2003]. However, it is also known that the majority of saturation change occurs at early time [*Gerhard and Kueper*, 2003] and the CMT images were visually inspected for fluid movement. In the few cases that fluid movement was observed in the images, the system was allowed to equilibrate until fluid movement was no longer observed. Thus, it was assumed that the system was at near-equilibrium conditions for all $P_c - S_w$ points. The CMT image data consisted of scanning a 5.5 mm section in the middle of the column at a resolution of $13 \text{ }\mu\text{m/voxel}$. The imaged region and the experimental setup are illustrated in Figure 2.

2.2. Image Analysis

[10] Gray-scale CMT images require further image analysis to accurately quantify phase distributions and fluid-fluid IFA. The wetting-, nonwetting- and solid-phase volume fractions were quantified via a segmentation routine and IFA was quantified using the commercially available image analysis software Avizo™. Details regarding our segmentation algorithm and its validation are available in the work of *Porter and Wildenschild* [2010]. The segmented data consists of three integer values (ternary), each representing a single phase. Porosity and saturation values were quantified by counting the voxels for each phase in the segmented data, and the resulting porosity of the imaged section was 0.36.

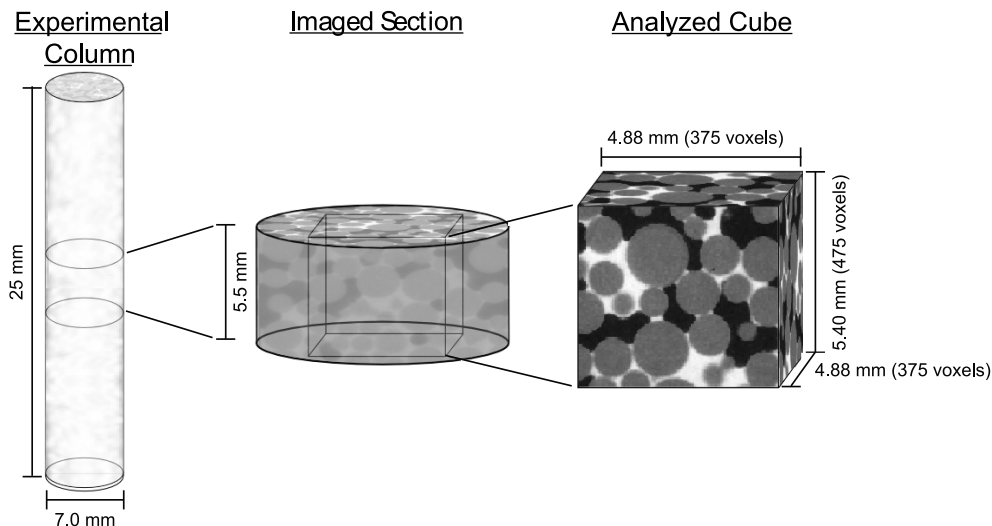


Figure 2. Illustration of the experimental column and sub-volumes from which S_w and IFA were measured.

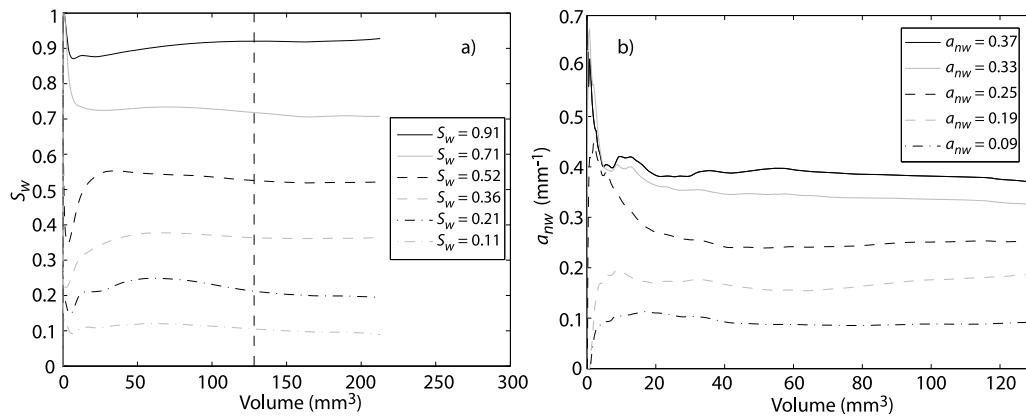


Figure 3. REV analysis for a subset of (a) S_w and (b) a_{nw} values. The vertical lines represent the volume of the cube that was analyzed in section 3.

[11] In order to distinguish between the bulk wetting-phase and pendular rings (see Figure 5) we used the IDL™ LABEL_REGION function to consecutively label all of the disconnected regions of each wetting-phase binary data set. Technically, the wetting-phase is fully connected via films; however, films are not resolved at a resolution of 13 μm , thus the wetting-phase appears disconnected in the CMT images. It was assumed that the regions connected to the bottom of the imaged column section (where the water enters and exits the section) represent bulk wetting-phase, whereas the remaining regions were considered to be pendular rings. It is acknowledge that this criteria does not guarantee that the identified bulk wetting-phase is connected to the outlet of the column; therefore, it was visually confirmed that the identified bulk wetting-phase exhibited a funicular pattern that spanned the entire length of the imaged section in every instance. Furthermore, it was visually confirmed that the bulk wetting-phase swelled between successive imbibition points, whereas the pendular rings did not show any significant increase in size, suggesting that the bulk wetting-phase was indeed connected to the outlet of the column.

[12] The total interfacial area for the solid phase, a_s , wetting-phase, a_w , and nonwetting-phase, a_n , was estimated via a generalized marching cubes algorithm in Avizo™, which generates isosurfaces between phases based upon a single isovalue chosen to separate one phase from the other phases. In this analysis the ternary data was mapped into three binary images, one for each phase, and then smoothed with a Gaussian filter ($3 \times 3 \times 3$ kernel) prior to constructing the isosurfaces. The isovalue for each isosurface was set to 0.5, which is half of the maximum and minimum values in each binary data set. Estimates of a_{nw} were calculated using the following equation [Montemagno and Ma, 1999; Dalla et al., 2002]

$$a_{nw} = \frac{1}{2}(a_w + a_n - a_s) \quad (1)$$

[13] Due to the relatively small size of the imaged section, we performed a representative elementary volume (REV) analysis for S_w , a_{nw} , a_n , and porosity. The REV analysis consisted of calculating these values for volumes ranging from approximately 6×10^{-5} - 213 mm^3 . Figure 3 shows

the REV analysis for the subset of S_w and a_{nw} values. The vertical lines in Figure 3 represent the volume (128 mm^3) of the cube analyzed in section 3. The REV analysis for S_w (Figure 3a) illustrates that S_w is essentially constant for volumes near 128 mm^3 implying that the cube is an REV. Furthermore, no significant changes in S_w are observed due to the presence of the column walls (213 mm^3 corresponds to the entire imaged section of the column), thus edge effects are considered to be small. The REV analysis for a_{nw} (Figure 3b) clearly shows that the a_{nw} values also vary little as the volume approaches that of the cube, indicating that the cube indeed comprises an REV for a_{nw} as well. Estimates of a_{nw} for volumes larger than the analyzed cube are not shown since the column wall introduces a fourth phase in the interfacial area calculation. It is noted that the cube is an REV for a_n and porosity; however, this is not shown.

2.3. Explicit IFA Model

[14] Grant and Gerhard [2007a] developed the Explicit IFA model, which is an extension of the thermodynamic model presented by Leverett [1941]. The thermodynamic approach hypothesizes that for a given S_w value, a_n can be calculated according to [Leverett, 1941]:

$$a_n(S_w) = \phi \frac{\Phi_{nw}(S_w)}{\sigma_{mw}}, \quad S_r < S_w \leq 1.0 \quad (2)$$

where ϕ is the porosity, σ_{mw} is the interfacial tension between the aqueous phase and the NAPL, and $\Phi_{nw}(S_w)$ is the area under the $P_c - S_w$ curve:

$$\Phi_{nw}(S_w) = - \int_X^{S_w} P_c(S_w) dS_w \quad (3)$$

Here X is equal to the value of S_w when $P_c = 0$, and $P_c(S_w)$ is the capillary pressure-saturation function for drainage or imbibition. In order to provide a model that can predict a_{nw} for all possible S_w values and be incorporated into multi-phase flow and transport models, the Explicit IFA model incorporates five modifications to the basic thermodynamic model: (1) incorporating the Gerhard and Kueper [2003] hysteretic constitutive functions, which were validated for NAPL migration in heterogeneous porous media by Grant et al. [2007], (2) implementing continuity of saturation

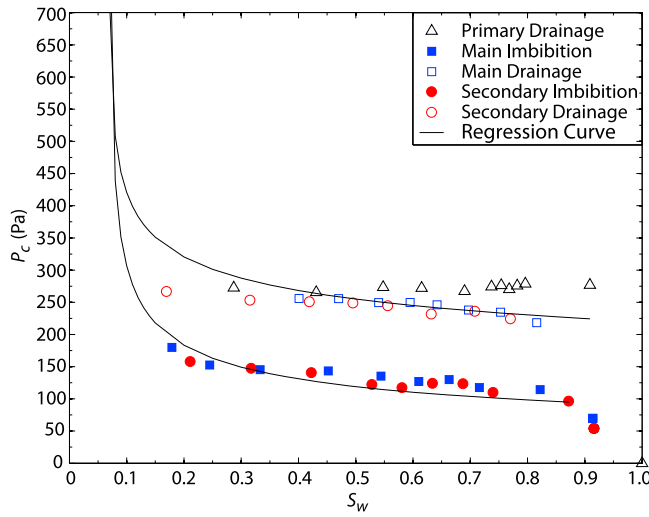


Figure 4. Hysteretic $P_c - S_w$ curves for the NAPL-water-glass bead system. Drainage and imbibition are represented by the open and solid symbols, respectively. The solid line was obtained using equations (5) and (6). The lowest S_w values (corresponding to P_c values of approximately 1900 Pa) are not shown here in order to preserve the vertical resolution.

history at all saturation reversal points, (3) conversion of a_n to a_{nw} using a saturation-dependent function derived from primary drainage data reported by *Dalla et al.* [2002], (4) accounting for energy losses via an energy dissipation factor, E_d , obtained by calibration to the data of *Brusseau et al.* [2006], and (5) implementation of an $a_{nw} - S_w$ relationship for the dissolution of residual NAPL.

[15] The Explicit IFA model is summarized as [*Grant and Gerhard, 2007a*]:

$$a_{nw}(S_w^i) = \Psi(S_w^i) \cdot E_d \cdot \phi \frac{[\Phi_{nw}(S_w)]^{D, I^*, D^*}}{\sigma_{nw}} \quad (4)$$

where Ψ is the ratio of a_{nw}/a_n that was obtained by calibration to data reported by *Dalla et al.* [2002] and S_w^i is the current S_w value. The superscripts D , I^* and D^* denote primary drainage, main imbibition and all subsequent imbibition events, and main drainage and all other drainage events, respectively. Thus, the model is able to predict both a_n and a_{nw} for any $P_c - S_w$ curve and any saturation history. Further details regarding equation (4) can be found in the work of *Grant and Gerhard* [2007a, equations (12)–(15)].

[16] The model employs the *Gerhard and Kueper* [2003] constitutive relationships, which are extensions of the *Brooks and Corey* [1964] $P_c - S_w$ relationship that account for complex S_w history. The primary drainage curve is defined as [*Gerhard and Kueper, 2003*]:

$$P_c = P_E \left(S_e^{-\lambda_d^{-1}} \right) \quad (5)$$

where P_E is the entry (displacement) pressure defined by the extension of the primary drainage curve to $S_w = 1.0$, λ_d is the pore-size distribution index associated with drainage processes, and $S_e = \frac{S_w - S_r}{1 - S_r}$ is the effective wetting phase saturation, in which S_r is the wetting phase residual satu-

ration parameter corresponding to infinite P_c . The main imbibition curve, which results if the minimum possible S_w was attained on primary drainage, is defined by a modified form of the drainage curve [*Gerhard and Kueper, 2003*]:

$$P_c = P_T \left(\frac{S_w - S_r}{S_w^{*\lambda_i} - S_r} \right)^{-\lambda_i^{-1}} \quad (6)$$

where P_T is the terminal capillary pressure, λ_i is the imbibition pore-size distribution index, and $S_w^{*\lambda_i}$ is the maximum nonwetting-phase residual S_w value. Further details (e.g., for scanning curves) are provided by *Gerhard and Kueper* [2003]. Relevant to this work, the parameters P_E , P_T , λ_d , λ_i , $S_w^{*\lambda_i}$ and S_r are best-fit to the measured $P_c - S_w$ data.

[17] The Explicit IFA model therefore relies only on the independently measured $P_c - S_w$ parameters, porosity, and fluid-fluid interfacial tension in order to predict a_n and a_{nw} for any S_w value. Predicted $a_{nw} - S_w$ was demonstrated by *Grant and Gerhard* [2007a] to reproduce both the magnitude and the shape of measured $a_{nw} - S_w$ data, including the peak interfacial area at $0.2 < S_w < 0.3$. Furthermore, the model was found to reproduce negligible a_{nw} at S_r and the observed hysteresis of $a_{nw} - S_w$ [*Grant and Gerhard, 2007a*]. Moreover, the predicted a_{nw} values were found useful for predicting the dissolution of pooled and residual NAPL in heterogeneous porous media [*Grant and Gerhard, 2007b*]. Note that the model's assumed relationship between a_{nw} and S_w for the dissolution of residual NAPL is not evaluated in this work.

[18] The method of *Brusseau et al.* [2006] is employed in this work to develop experimental relationships of $P_c - S_w - a_{nw}$ and $P_c - S_w - a_n$. The column $P_c - S_w$ data was best-fit with the *Gerhard and Kueper* [2003] hysteretic constitutive relationships (i.e., modified Brooks-Corey). These relationships were then used to determine P_c for each $a_n - S_w$ and $a_{nw} - S_w$ pair measured on the cube (Figure 2). This coupling of the two data sets at different scales via the S_w value assumes that (1) the cube is an REV with respect to P_c , which is reasonable since it was shown to be an REV for both S_w and a_{nw} (section 2.2), and (2) that the $P_c - S_w$ relationships for the column and the cube are similar.

3. Results and Discussion

3.1. Capillary Pressure–Saturation Curves

[19] The drainage and imbibition $P_c - S_w$ curves for the column are shown in Figure 4. Excellent repeatability is observed on drainage and imbibition cycles beyond primary drainage; it is hypothesized that the latter is less representative of the REV because the nonwetting-phase has not penetrated the length of the entire column at high S_w values. The best-fit parameters to the data, presented in Table 2, were therefore determined with the primary drainage values omitted. The entry pressure and high pore size distribution indices are in the range of values for sand with similar grain

Table 2. Best Fit Parameters for the Modified Brooks and Corey Regression Curves

P_E	P_T	λ_d	λ_i	$S_w^{*\lambda_i}$	S_r
220 Pa	90.0 Pa	5.2	7.5	0.91	0.07

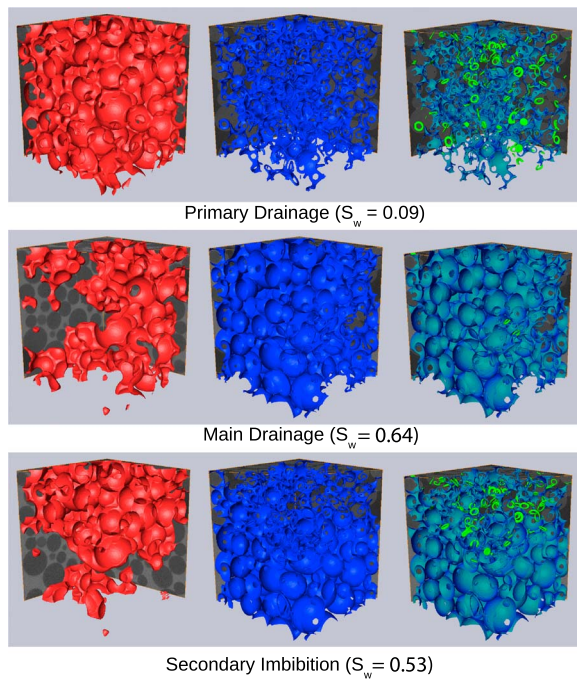


Figure 5. Examples of the isosurfaces used to calculate a_{nw} . (left) The nonwetting-phase (red), (middle) the wetting-phase (blue), and (right) both the bulk wetting-phase (blue-green) and wetting-phase pendular rings (green).

size distributions (e.g., medium to coarse) [Brooks and Corey, 1964; Liu et al., 1998; Oostrom and Lenhard, 1998].

3.2. Interfacial Area Estimates

[20] A few examples of the nonwetting- and wetting-phase isosurfaces used to estimate IFA are shown in Figure 5. The isosurfaces shown represent primary drainage, main drainage, and secondary imbibition. The wetting-phase isosurface for primary drainage shows the existence of numerous pendular rings and wetting-phase bridges at a saturation of 0.09. Figure 5 (right) shows the portion of the wetting-phase isosurface associated with pendular rings and that associated with the bulk wetting-phase, demonstrating that even at low saturations the wetting-phase was relatively well connected in funicular patterns. In fact, approximately 80% of the water at $S_w = 0.09$ is associated with the bulk

wetting phase. During main drainage very few pendular rings have formed at $S_w = 0.64$, whereas during imbibition numerous pendular rings are still present at $S_w = 0.53$.

[21] Figure 6 shows the measured $a_n - S_w$ and $a_{nw} - S_w$ curves. Clearly, a_n in Figure 6a is a linear function of S_w that tends toward the solid surface area ($a_s = 3.75 \text{ mm}^{-1}$) as S_w decreases. The shape and magnitude of this curve is consistent with other experimentally measured curves [e.g., Kim and Rao, 1997; Anwar et al., 2000; Costanza-Robinson et al., 2008] for similar porous media. It is interesting to note that virtually no hysteresis is observed in the $a_n - S_w$ curves in Figure 6a. This result is somewhat unexpected since hysteresis is observed in Figure 6b. The shape and magnitude of the $a_{nw} - S_w$ curves are consistent with curves observed in other CMT experiments [Culligan et al., 2004, 2006; Brusseau et al., 2007] and predicted by pore-scale numerical models [Reeves and Celia, 1996; Held and Celia, 2001; McClure et al., 2004; Joekar-Niasar et al., 2007; Porter et al., 2009].

3.3. Experimental Constitutive Relationship

[22] For the sake of consistency with existing publications [Joekar-Niasar et al., 2007, 2009; Porter et al., 2009], the $P_c - S_w - a_n$ and $P_c - S_w - a_{nw}$ relationships were characterized by fitting a bi-quadratic polynomial to the experimental data. The best-fit $P_c - S_w - a_n$ (RMSE = 0.03 mm^{-1}) and $P_c - S_w - a_{nw}$ (RMSE = 0.02 mm^{-1}) surfaces are shown in Figure 7. The best-fit surfaces represent only the main branches of the $P_c - S_w$ curves since scanning curves were not measured. The extent to which the shape of the surfaces would be affected by the inclusion of scanning curve data is unknown. However, it has been shown using lattice-Boltzmann simulations (validated with CMT image data) that the $P_c - S_w - a_{nw}$ surfaces obtained with and without scanning curves (for an air-water system) exhibited minor differences [Porter et al., 2009]. The $P_c - S_w - a_n$ surface does not exhibit curvature along the P_c - or S_w -axis; it is simply a plane bounded by the P_c and S_w values. The $P_c - S_w - a_{nw}$ surface exhibits some convex curvature along the P_c -axis over the entire range of S_w values. This is consistent with the shape of the surfaces simulated by Porter et al. [2009] and Joekar-Niasar et al. [2007, 2009] at high S_w values. In the experiments reported here the drainage $a_{nw} - S_w$ curves are higher than the imbibition curves, whereas the lattice-Boltzmann [Porter et al., 2009] and pore network [Joekar-Niasar et al., 2007] simulations

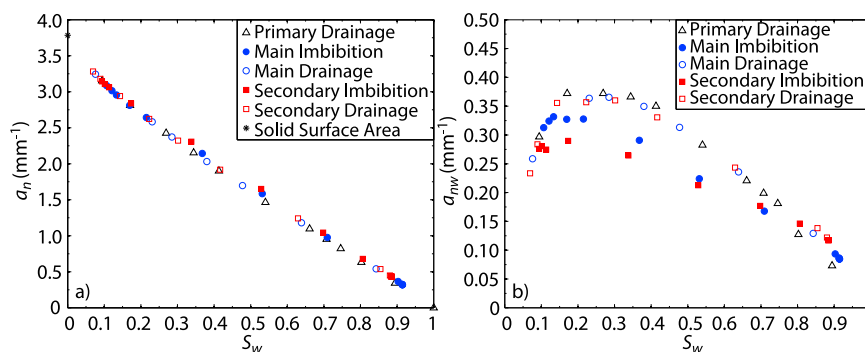


Figure 6. Experimental interfacial area curves for (a) $a_n - S_w$ and (b) $a_{nw} - S_w$. The open symbols represent drainage, whereas the solid symbols represent imbibition.

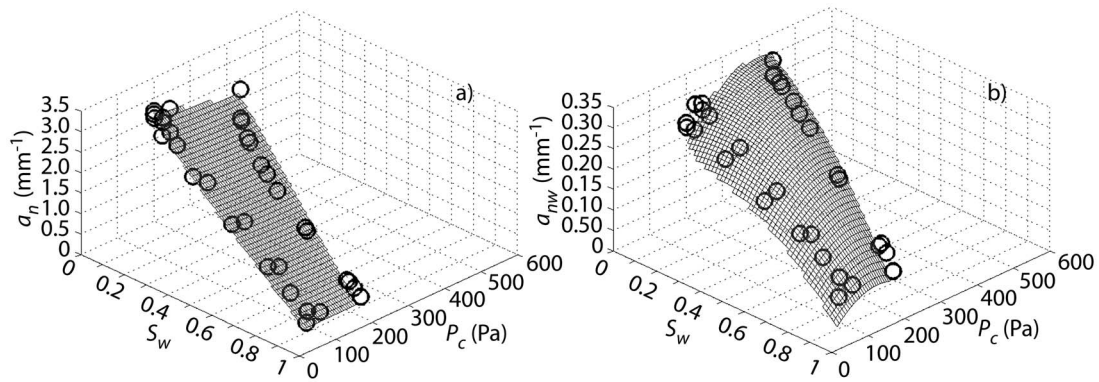


Figure 7. Best-fit surfaces for the experimental (a) $P_c - S_w - a_n$ and (b) $P_c - S_w - a_{nw}$ data. The open circles represent the measured data.

predict imbibition $a_{nw} - S_w$ curves that are higher than drainage curves. In addition, the magnitude of the surfaces are similar to those presented by Porter *et al.* [2009], but smaller (by a maximum factor of approximately 3) than those reported by Joekar-Niasar *et al.* [2007]. Note that the a_{nw} values reported by Joekar-Niasar *et al.* [2007] range over an order of magnitude depending upon the displacement rules and porous media configurations, thus the magnitude differences observed between those simulations and the data reported here are most likely due to differences in the modeled system.

[23] An interesting observation can be made about hysteresis in the $P_c - S_w - a_n$ relationship. Based on the fact that no hysteresis was observed in the $a_n - S_w$ curves (see Figure 6a), the scanning curves for a_n would all lie on the same curve and thus fill in the surface (Figure 7a) along the same plane, indicating that a unique surface (i.e., one that exhibits negligible hysteresis) describes the $P_c - S_w - a_n$ relationship. This result is in contrast to IFFT experiments reported by Chen and Kibbey [2006] in which hysteresis was observed for successive drainage $a_n - S_w$ curves.

3.4. Explicit IFA Model Comparison

[24] Figure 8 compares the projection of a_n onto the $P_c - S_w$ plane for the experiments and Explicit IFA model

predictions, as well as the absolute error between the two surfaces. This format is employed here in preference to the format of Figure 7 in order to permit better visualization of the comparison. The predicted surface was generated using primary drainage, main imbibition, and main drainage constitutive functions, which is consistent with the data used to create the experimental surface. Figure 8 reveals that the magnitude of a_n is quite similar between the two surfaces, with a mean absolute error of 0.19 mm^{-1} (RMSE = 0.30 mm^{-1}). The maximum absolute error (1.03 mm^{-1}) only occurs in a small region representing S_w of approximately 0.3 and P_c of approximately 150 Pa, while the majority of the surface is characterized by an absolute error of less than 0.35 mm^{-1} . In addition, an error of up to 0.86 mm^{-1} is observed in the region associated with nonwetting-phase residual saturation. The experimental a_n values at the end of imbibition are approximately 0.3 mm^{-1} (representing a few large NAPL ganglia), whereas the predicted a_n at the end of imbibition is approximately 1.1 mm^{-1} (representing numerous, small disconnected NAPL blobs). Prediction of a significant amount of a_n associated with residual NAPL is inherent in thermodynamic-based models [e.g., Grant and Gerhard, 2007a; Schroth *et al.*, 2008] due to the significant difference in the work done on the system to drain versus to imbibe wetting-phase. A discrepancy is also noted between the shapes of the two surfaces: the experimental surface represents a flat plane in $P_c - S_w$

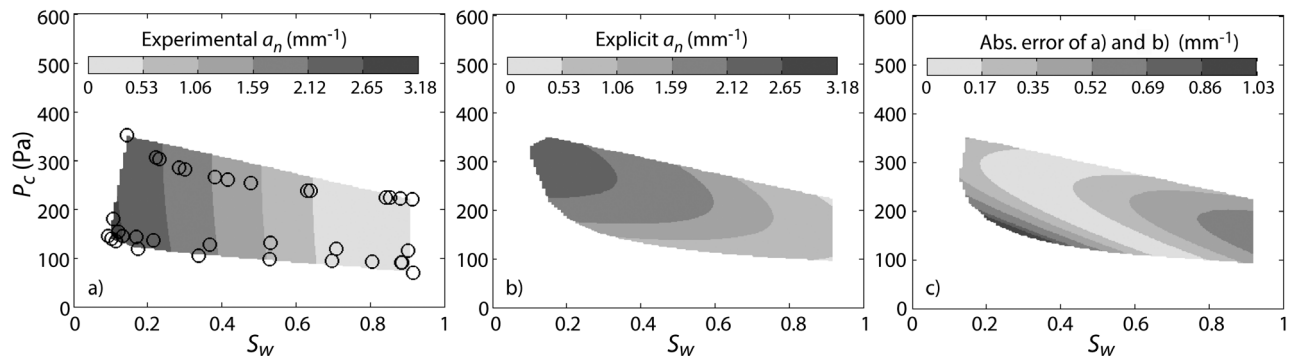


Figure 8. Projection of the $P_c - S_w - a_n$ surface onto the $P_c - S_w$ plane for (a) the experimental surface, (b) the Explicit IFA model surface, and (c) the absolute error between the experimental and Explicit IFA model surfaces.

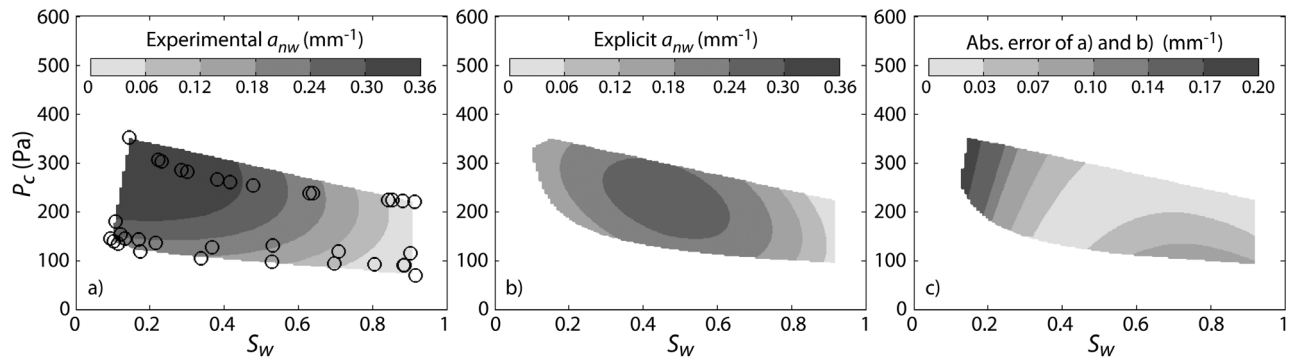


Figure 9. Projection of the $P_c - S_w - a_{nw}$ surface onto the $P_c - S_w$ plane for (a) the experimental surface, (b) the Explicit IFA model surface without scanning curves, and (c) the absolute error between the experimental and Explicit IFA model surfaces.

space, whereas the predicted surface exhibits convex curvature in the P_c -axis. This curvature is primarily due to the fact that a_n values predicted by thermodynamic models are hysteretic between drainage and imbibition events.

[25] Figure 9 compares the projection of a_{nw} onto the $P_c - S_w$ plane for the experiments and Explicit IFA model predictions. Once again, the data used to generate the predicted surface includes primary drainage, main imbibition, and main drainage. There is good correspondence between the magnitudes of a_{nw} for the experiments and predictions. The maximum absolute error (0.20 mm^{-1}) occurs in a small region at low S_w values, with a mean absolute error for the entire surface of 0.04 mm^{-1} (RMSE = 0.06 mm^{-1}). The maximum difference at high S_w values is 0.10 mm^{-1} and corresponds to discrepancies in the morphology of residual nonwetting-phase. There are also discrepancies between the shape of the experimental and predicted $P_c - S_w - a_{nw}$ surfaces. The predicted a_{nw} surface in Figure 9b exhibits more pronounced convex curvature along the P_c -axis than observed in the experimental surface. In addition, the predicted surface peaks with a maximum $a_{nw} = 0.30 \text{ mm}^{-1}$ at S_w values ranging from 0.35–0.60, whereas the experimental surface peaks with a maximum $a_{nw} = 0.36 \text{ mm}^{-1}$ at S_w values ranging from 0.10–0.45. The differences in the shapes of the experimental and predicted surface can, in part, be explained by differences in the relative magnitudes of successive $a_{nw} - S_w$ curves. The experiments consistently show

all drainage $a_{nw} - S_w$ curves higher than all imbibition curves, whereas the Explicit IFA model predicts this for main drainage but predicts lower a_{nw} for the primary drainage curve (due to the absence of residual non-wetting phase).

[26] Figure 10 highlights the influence of scanning curves on the magnitude and shape of the predicted surface and their affect on the comparison between the experimental and modeled surfaces. Thus, the data used to create the surface in Figure 10b includes primary drainage, main imbibition, and main drainage, as well as 16 drainage and 16 imbibition scanning curves (corresponding to turnaround S_w values at 0.05 increments across the range of $0.1 < S_w < 0.85$). The inclusion of the scanning curves affects the shape of the surface most notably a low P_c values over the entire range of S_w values. Figure 10c indicates that the maximum absolute error is 0.20 mm^{-1} in a very small region at low S_w values; however, over the majority of the surface the mean absolute error is less than 0.07 mm^{-1} . Thus, overall, the predicted magnitude of the $P_c - S_w - a_{nw}$ surface is very good. In fact the mean absolute error between these two surfaces is 0.04 mm^{-1} (RMSE = 0.06 mm^{-1}), the same as obtained with the surface that did not include scanning curve data. Clearly, the addition of the scanning curve data has caused the formation of a saddle; the surface is convex along the S_w -axis and slightly concave along the P_c -axis at mid-range S_w values. Interestingly, the shape of this predicted surface is

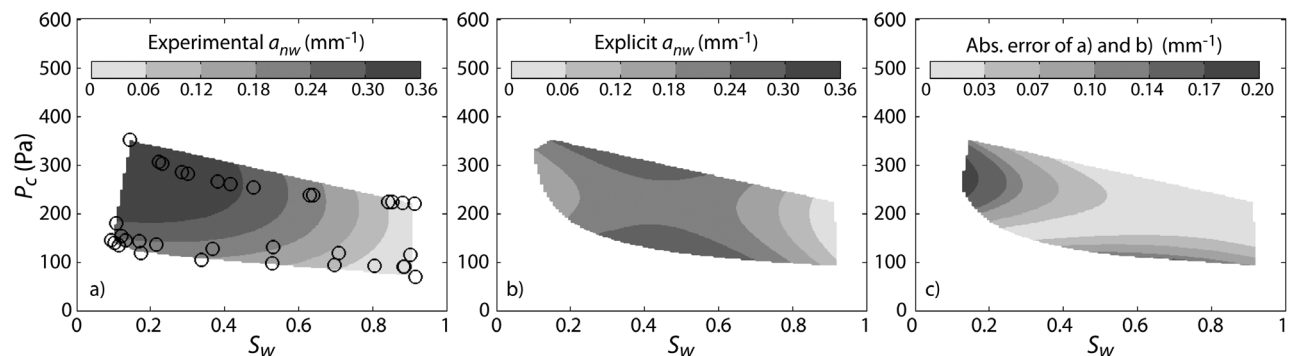


Figure 10. Projection of the $P_c - S_w - a_{nw}$ surface onto the $P_c - S_w$ plane for (a) the experimental surface, (b) the Explicit IFA model surface with scanning curves, and (c) the absolute error between the experimental and Explicit IFA model surfaces.

similar to the pore network model surface presented by Joekar-Niasar et al. [2007].

4. Conclusions

[27] In this study, the $P_c - S_w - a_n$ and $P_c - S_w - a_{nw}$ relationships were characterized using CMT imaging data for NAPL-water drainage and imbibition experiments, and subsequently modeled using the Explicit IFA model [Grant and Gerhard, 2007a]. Image analysis of the CMT data indicated that at low S_w values the majority of the wetting-phase (80% or more) consisted of a few funicular paths that spanned the length of the imaged section, whereas the remaining wetting-phase consisted of numerous pendular rings. Both the $a_n - S_w$ and $a_{nw} - S_w$ curves were consistent with those reported in the literature. Moreover, the experimental $a_n - S_w$ curves indicated that hysteresis was not observed in a_n .

[28] A bi-quadratic polynomial was used to characterize the $P_c - S_w - a_n$ and $P_c - S_w - a_{nw}$ relationships. The resulting best-fit experimental surfaces were similar in magnitude and shape with those previously reported in the literature, and specific differences were consistent with differences in the fluid distributions. In addition, it was shown that hysteresis in the experimental $P_c - S_w - a_n$ relationship is negligible based on the fact that the $a_n - S_w$ curves were all on the same line.

[29] Comparisons between the experiments and the Explicit IFA model revealed that, as a whole, the model is capable of reproducing the magnitudes of both $P_c - S_w - a_n$ and $P_c - S_w - a_{nw}$ surfaces. The most notable differences occurred in regions associated with the wetting- and non-wetting-phase residual saturations. Thermodynamic models will inherently have difficulty reproducing experimental data that exhibits values of a_n and a_{nw} for residual NAPL that is less than those for primary drainage at the same S_w values. Experimental systems for measuring P_c , S_w , a_n and a_{nw} , and constitutive relationships based on those data, are known to be less representative of REV's at the function extremities. In addition, there were discrepancies between the shapes of the experimental and predicted surfaces. These discrepancies are attributed, in part, to the primary drainage $a_n - S_w$ and $a_{nw} - S_w$ pathway present in the model that is unique from the main imbibition-main drainage closed loop. It is further acknowledged that the experimental data does not include scanning curves which may alter the shape of the surface.

[30] Overall, the Explicit IFA predicted $P_c - S_w - a_n$ and $P_c - S_w - a_{nw}$ results are encouraging since the model provides a practical tool for constructing these surfaces from any measured or estimated $P_c - S_w$ curve. In so doing, it provides the opportunity to avoid characterizing all soil types and fluid pairs via expensive imaging techniques. Further research is needed in order to define the influence of scanning curves on the experimental surfaces, particularly to confirm the absence of hysteresis in the surface. It is acknowledged that additional validation of thermodynamic models against more complex and representative systems would be valuable. Further research is also required to (1) determine the model validity and appropriate model parameters across a wider range of fluid-fluid-porous media systems, and (2) explore the value of thermodynamic models to advance the simulation of interfacial area-

dependent phenomena at the field scale, such as NAPL source zone dissolution and NAPL-aqueous phase reaction kinetics (e.g., in situ chemical oxidation).

[31] **Acknowledgments.** Porter and Wildenschild were supported by NSF-EAR-06101108 and NSF-EAR-0337711. We thank Kendra Brown for her assistance with the experiments at Argonne National Lab and in the laboratory at Oregon State University. A portion of this work was conducted at GeoSoilEnviroCARS (Sector 13), Advanced Photon Source (APS), Argonne National Laboratory. GeoSoilEnviroCARS is supported by the National Science Foundation-Earth Sciences (EAR-0622171) and Department of Energy-Geosciences (DE-FG02-94ER14466). Use of the Advanced Photon Source was supported by the U.S. Department of Energy, Office of Science, Office of Basic Energy Sciences, under contract DE-AC02-06CH11357. We thank Mark Rivers and the entire staff at GSECARS for experimental support.

References

- Anwar, A., M. Bettahar, and U. Matsubayashi (2000), A method for determining air-water interfacial area in variably saturated porous media, *J. Contam. Hydrol.*, *43*, 129–146.
- Bradford, S. A., and F. J. Leij (1997), Estimating interfacial areas for multi-fluid soil systems, *J. Contam. Hydrol.*, *27*, 83–105.
- Brooks, R. H., and A. T. Corey (1964), Hydraulic properties of porous media, in *Hydrology Papers*, Colo. State Univ., Ft. Collins.
- Brusseau, M. L., S. Peng, G. Schnaar, and M. S. Costanza-Robinson (2006), Relationship among air-water interfacial area, capillary pressure and water saturation for a sandy porous medium, *Water Resour. Res.*, *42*, W03501, doi:10.1029/2005WR004058.
- Brusseau, M. L., S. Peng, G. Schnaar, and A. Murao (2007), Measuring air-water interfacial areas with X-ray microtomography and interfacial partitioning tracer tests, *Environ. Sci. Technol.*, *41*, 1956–1961.
- Bryant, S. L., and A. S. Johnson (2004), Bulk and film contributions to fluid/fluid interfacial area in granular media, *Chem. Eng. Commun.*, *191*, 1660–1670.
- Chen, D., L. J. Pyrak-Nolte, J. Griffin, and N. J. Giordano (2007), Measurement of interfacial area per volume for drainage and imbibition, *Water Resour. Res.*, *43*, W12504, doi:10.1029/2007WR006021.
- Chen, L., and C. Kibbey (2006), Measurement of air-water interfacial area for multiple hysteretic drainage curves in an unsaturated fine sand, *Langmuir*, *22*(16), 6874–6880.
- Cheng, J.-T., L. J. Pyrak-Nolte, D. D. Nolte, and N. J. Giordano (2004), Linking pressure and saturation through interfacial areas in porous media, *Geophys. Res. Lett.*, *31*, L08502, doi:10.1029/2003GL019282.
- Costanza-Robinson, M. S., K. H. Harrold, and R. M. Lieb-Lappen (2008), X-ray microtomography determination of air-water interfacial area-water saturation relationships in sandy porous media, *Environ. Sci. Technol.*, *42*(8), 2949–2956.
- Culligan, K. A., D. Wildenschild, B. S. Christensen, W. G. Gray, M. L. Rivers, and A. B. Tompson (2004), Interfacial area measurements for unsaturated flow through porous media, *Water Resour. Res.*, *40*, W12413, doi:10.1029/2004WR003278.
- Culligan, K. A., D. Wildenschild, B. S. Christensen, W. G. Gray, and M. L. Rivers (2006), Pore-scale characteristics of multiphase flow in porous media: A comparison of air-water and oil-water experiments, *Adv. Water Resour.*, *29*, 227–238.
- Dalla, E., M. Hilpert, and C. T. Miller (2002), Computation of the interfacial area for two-fluid porous systems, *J. Contam. Hydrol.*, *56*, 25–48.
- Dobson, R., M. H. Schroth, M. Oostrom, and J. Zeyer (2006), Determination of NAPL-water interfacial areas in well-characterized porous media, *Environ. Sci. Technol.*, *40*, 815–822.
- Gerhard, J. I., and B. H. Kueper (2003), Capillary pressure characteristics necessary for simulating DNAPL infiltration, redistribution, and immobilization in saturated porous media, *Water Resour. Res.*, *39*(8), 1212, doi:10.1029/2002WR001270.
- Gladkikh, M., and S. Bryant (2003), Prediction of interfacial areas during imbibition in simple porous media, *Adv. Water Resour.*, *26*, 609–622.
- Grant, G. P., and J. I. Gerhard (2007a), Simulating the dissolution of a complex dense nonaqueous phase liquid source zone: 1. Model to predict interfacial area, *Water Resour. Res.*, *43*, W12410, doi:10.1029/2007WR006038.

- Grant, G. P., and J. I. Gerhard (2007b), Simulating the dissolution of a complex dense nonaqueous phase liquid source zone: 2. Experimental validation of an area-based mass transfer model, *Water Resour. Res.*, *43*, W12409, doi:10.1029/2007WR006039.
- Grant, G. P., J. I. Gerhard, and B. H. Kueper (2007), Multidimensional validation of a numerical model for simulating a DNAPL release in heterogeneous porous media, *J. Contam. Hydrol.*, *92*, 109–128.
- Gray, W. G. (2000), Macroscale equilibrium conditions for two-phase flow in porous media, *Int. J. Multiphase Flow*, *26*, 467–501.
- Hassanizadeh, M. S., and W. G. Gray (1993), Thermodynamic basis of capillary pressure in porous media, *Water Resour. Res.*, *29*(10), 3389–3405.
- Held, R. J., and M. A. Celia (2001), Modeling support of functional relationships between capillary pressure, saturation, interfacial area and common lines, *Adv. Water Resour.*, *24*, 325–343.
- Helland, J., and S. Skjæveland (2007), Relationship between capillary pressure, saturation, and interfacial area from a model of mixed-wet triangular tubes, *Water Resour. Res.*, *43*, W12S10, doi:10.1029/2006WR005698.
- Joekar-Niasar, V., S. M. Hassanizadeh, and A. Leijnse (2007), Insights into the relationship among capillary pressure, saturation, interfacial area and relative permeability using pore-network modeling, *Transp. Porous Med.*, *74*(2), 201–219.
- Joekar-Niasar, V., S. M. Hassanizadeh, L. Pyrak-Nolte, and C. Berentsen (2009), Simulating drainage and imbibition experiments in a high porosity micromodel using an unstructured pore-network model, *Water Resour. Res.*, *45*, W02430, doi:10.1029/2007WR006641.
- Kim, H., and P. S. C. Rao (1997), Determination of effective air-water interfacial area in partially saturated porous media using surfactant adsorption, *Water Resour. Res.*, *33*(12), 2705–2711.
- Leverett, M. (1941), Capillary behavior in porous solids, *Trans. Am. Inst. Min. Metall. Pet. Eng.*, *142*, 152–169.
- Liu, Y., J. W. Hopmans, M. Grismer, and J. Chen (1998), Direct estimation of air-oil and oil-water capillary pressure and permeability relations from multi-step outflow experiments, *J. Contam. Hydrol.*, *32*, 223–245.
- McClure, J., C. Pan, D. Adalsteinsson, W. Gray, and C. Miller (2004), Estimating interfacial areas resulting from lattice-Boltzmann simulation of two-fluid-phase flow in a porous medium, in *Computational Methods in Water Resources XV*, vol. 1., edited by C. T. Miller et al., Elsevier, New York.
- Miller, C. T., G. Christakos, P. T. Imhoff, J. F. McBride, J. A. Pedit, and J. A. Trangenstein (1998), Multiphase flow and transport modeling in heterogeneous porous media: Challenges and approaches, *Adv. Water Resour.*, *21*(2), 77–120.
- Montemagno, C. D., and Y. Ma (1999), Measurement of interfacial surface areas for two-phase flow in porous media from PVI data, in *Characterization and Measurements of Hydraulic Properties of Unsaturated Porous Media*, edited by M. T. van Genuchten, F. Leijde, and L. Wu, pp. 121–132, University of Calif. Press, Riverside.
- Morrow, N. R. (1970), Physics and thermodynamics of capillary action in porous media, *Ind. Eng. Chem.*, *62*(6), 32–56.
- Muccino, J. C., W. G. Gray, and L. A. Ferrand (1998), Toward an improved understanding of multiphase flow in porous media, *Rev. Geophys.*, *36*(3), 401–422.
- Oostrom, M., and R. J. Lenhard (1998), Comparison of relative permeability-saturation-pressure parametric models for infiltration and redistribution of a light nonaqueous-phase liquid in sandy porous media, *Adv. Water Resour.*, *21*(2), 145–157.
- Porter, M. L., and D. Wildenschild (2010), Image analysis algorithms for estimating porous media multiphase flow variables from computed microtomography data: A validation study, *Comput. Geosci.*, *14*(1), 15–30, doi:10.1007/s10596-009-9130-5.
- Porter, M. L., M. G. Schaap, and D. Wildenschild (2009), Lattice-Boltzmann simulations of the capillary pressure-saturation-interfacial area relationship in porous media, *Adv. Water Resour.*, *32*(11), 1632–1640, doi:10.1016/j.advwatres.2009.08.009.
- Reeves, P. C., and M. A. Celia (1996), A functional relationship between capillary pressure, saturation and interfacial area as revealed by a pore-scale network model, *Water Resour. Res.*, *32*(8), 2345–2358.
- Schaap, M. G., M. L. Porter, B. S. Christensen, and D. Wildenschild (2007), Comparison of pressure-saturation characteristics derived from computed tomography images and lattice Boltzmann simulations, *Water Resour. Res.*, *43*, W12S06, doi:10.1029/2006WR005730.
- Schroth, M. H., M. Oostrom, R. Dobson, and J. Zeyer (2008), Thermodynamic model for fluid-fluid interfacial areas in porous media for arbitrary drainage-imbibition sequences, *Vadose Zone J.*, *7*(3), 966–971.
- Wildenschild, D., J. W. Hopmans, C. Vaz, M. L. Rivers, D. Rikard, and B. S. Christensen (2002), Using X-ray computed microtomography in hydrology: Systems, resolution and limitations, *J. Hydrol.*, *267*, 285–297.
- Wildenschild, D., J. W. Hopmans, M. L. Rivers, and A. J. Kent (2005), Quantitative analysis of flow processes in a sand using synchrotron-based X-ray microtomography, *Vadose Zone J.*, *4*, 112–126.

J. I. Gerhard, Department of Civil and Environmental Engineering, University of Western Ontario, London, ON N6A 5B9, Canada.

G. Grant, Geosyntec Consultants, 130 Research Ln., Ste. 2, Guelph, ON N1G 5G3, Canada.

M. L. Porter and D. Wildenschild, School of Chemical, Biological, and Environmental Engineering, Oregon State University, 102 Gleeson Hall, Corvallis, OR 97331, USA. (porterma@enr.orst.edu)